PERGAMON

International Journal of Heat and Mass Transfer 43 (2000) 341–351

International Journal of HEAT and MASS TRANSFER

www.elsevier.com/locate/ijhmt

Numerical analysis of solutal convection in rotating shallow electrochemical cells

F.-B. Weng, Y. Kamotani*, S. Ostrach

Department of Mechanical and Aerospace Engineering, Case Western Reserve University, Cleveland, OH 44106, USA

Received 20 November 1998; received in revised form 23 April 1999

Abstract

A numerical study of solutal convection in rotating shallow electrochemical cells is performed. Typical cases show complex interactions among the centrifugal, Coriolis forces and mass transfer process in the rotating cells, which depend on the *Ek* and *Sc* Ro_S numbers. At low rotational speed (*Ek* is near 0.01) the inviscid core flow is unicellular and sandwiched between the top and bottom Ekman layers. When *Ek* is less than about 0.006, a series of secondary cells are induced by the Coriolis force in the core. It is found that the Coriolis force suppresses the centrifugal convection, reducing the mass transfer rate, especially at low *Sc* Ro_S. The present numerical results are shown to be in good agreement with our earlier scaling analysis as well as with our experimental mass transfer data.

1. Introduction

The present work is a part of our continuous effort to investigate transport phenomena in rotating electrochemical systems. It is known that a rotating Ni/Zn battery can provide very high power density, long life-cycle at low material costs [1,2]. The main objective of our effort is to obtain a better understanding of convection in a rotating battery in order to improve Ni/Zn battery performance and life-cycle. The rotating Ni/Zn battery system can be considered as a rotating electrolyte solution (an excess KOH electrolyte solution containing zincate) inside a shallow electrochemical cell subjected to an axial concentration difference. The electrolyte solution has a uniform concentration before the charging process. It is in solid-body rotation with a radial pressure gradient caused by centrifugal acceleration. With superimposed rotating motion in the charging cell, the solutal buoyancy induces a swirling secondary flow through the coupling of the centrifugal, Coriolis, and gravitational accelerations as well as density variations in the electrolyte solution.

The dynamics of rotating fluids represent complex phenomena in fluid dynamics and attracted a great deal of attention in the past [3]. The problems that were investigated can be divided into two major groups, one dealing with homogenous fluids and the other with stratified rotating fluids. Homogenous systems are those in which motion of the fluid is induced by the viscous rotating boundary [4]. In stratified rotating fluids, the coupling of multiple body forces and density gradients induces a swirling secondary flow. A great deal of work has been done on rotating cylinders with radial density gradients because the configuration is important in meteorology [5]. Some attention has been given to rotating systems with axial density gradients, which is more closely related to the present rotating battery application.

In the present work, solutal convection is studied in

* Correspondence author. Tel.: +1-216-368-6455; fax: +1-216-368-6445.

E-mail address: yxk@po.cwru.edu (Y. Kamotani)

0017-9310/00/$ - see front matter
PII: S0017-9310(99)00149-0

Nomenclature

Ac	centrifugal acceleration level, $\Omega^2 R/g$	$\bar{u}$, u	dimensional and dimensionless r-component velocities
Ar	aspect ratio, H/R	$\bar{v}$, v	dimensional and dimensionless θ-component velocities
$\bar{C}$, C	Cu^{2+} ion dimensional and dimensionless concentrations	$\bar{w}$, w	dimensional and dimensionless z-component velocities
D	mass diffusion coefficient	$\bar{z}$, z	dimensional and dimensionless vertical coordinates
Ek	Ekman number, $\nu/\Omega H^2$	α	thermal diffusivity
g	gravitational acceleration	β	volumetric expansion coefficient due to concentration change
H	thickness of test cell	β_T	volumetric expansion coefficient due to temperature change
h_m	total mass transfer coefficient	ν	kinematic viscosity
$h_m(r)$	local mass transfer coefficient	ΔC	Cu^{2+} ion concentration difference between two electrodes
Pr	Prandtl number, ν/α	ΔT	temperature difference between two walls
$\bar{p}$, p	dimensional and dimensionless pressures	ρ	density
R	radius of test cell	ϕ	field variables
Ro_S	solutal Rossby number, $\beta\Delta C$	Ω	rotation speed
Ro_T	thermal Rossby number, $\beta_T\Delta T$		
$\bar{r}$, r	dimensional and dimensionless radial coordinates		
Sc	Schmidt number, ν/D		
$Sh(r)$	local Sherwood number, $h_m(r)H/D$		
$\overline{Sh}$	total Sherwood number, $h_m H/D$		

shallow vertical rotating electrochemical cells with different concentrations imposed at two electrodes (see Fig. 1). We have recently performed scaling analysis as well as experimentally investigated the convection and mass transfer rate in the same configuration [6]. Pertinent literature is reviewed in that paper. The scaling analysis finds two convection regimes and shows that the parameters Ek and $Sc\ Ro_S$ are important to determine the mass transfer rate. The parameter $Sc\ Ro_S$ determines the convection regime as well as the thickness ratio of viscous layer to solutal layer. The mass transfer rates measured in the experiment are in agreement with the scaling analysis. Due to difficulties in flow visualization and concentration measurement in the shallow rotating cells, no information about the flow and solutal fields other than the total mass transfer rate was obtained in our earlier experiment. Therefore, the problem is analyzed numerically in the present work in order to supplement the experiment and the scaling analysis. The thermal convection in rotating systems with axial density gradients has been analyzed numerically in the past [7,8]. The work by Guo and Zhang [7] is for an enclosure of unit aspect ratio and for air, so their results are not suitable for the present battery application. The work by Chew [8] is for low aspect ratio enclosures as in the present problem, and the parameter $Pr\ Ro_T$ (corresponding to $Sc\ Ro_S$ in mass transfer) is larger than unity in his computation for a high Prandtl number oil so that the flow is in the centrifugally driven convection regime, but only a few cases are investigated under those conditions. In the present work, the mass transfer in rotating shallow cylinders is investigated over wider ranges of Ek and $Sc\ Ro_S$ and in more details than in the work by Chew [8].

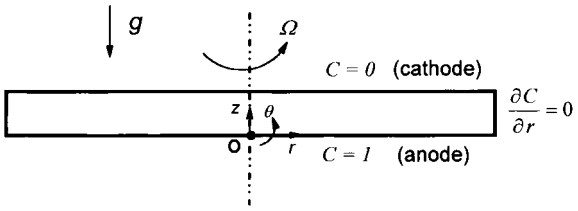

Fig. 1. Configuration of a rotating shallow electrochemical cell.

The main purpose of this numerical study is to obtain a physical insight into the nature of interactions among the centrifugal, Coriolis, and viscous forces. The detailed flow and solutal fields as well as local mass transfer rate are discussed in terms of parameters Ek and $Sc\ Ro_S$. The results from our earlier scaling analysis and experimental investigations of mass transfer are used to validate the numerical study.

2. Mathematical model and numerical calculation

A mathematical model is derived for the convective transport problem in a shallow rotating electrochemical cell. The following assumptions are made in the

model. The flow is steady, axisymmetric, and laminar. The fluid is incompressible and Newtonian with negligible viscous dissipation. The modified Boussinesq approximation is used, namely the density is variable only in the centrifugal and gravitational terms. The migration effect on the mass transport process is negligible in the presence of supporting fluid. The electrolyte solution is assumed to be dilute and isothermal.

The dimensionless variables and parameters used in the present analysis are:

$$r=\frac{\bar{r}}{R},\quad z=\frac{\bar{z}}{R},\quad u=\frac{\bar{u}}{\Omega R\left(\frac{\beta\Delta C}{Sc}\right)^{1/2}},$$

$$w=\frac{\bar{w}}{\Omega R\left(\frac{\beta\Delta C}{Sc}\right)^{1/2}},$$

$$v=\frac{\bar{v}}{\Omega R\left(\frac{\beta\Delta C}{Sc}\right)^{1/2}},\quad p=\frac{\bar{p}}{\rho\Omega^2R^2\left(\frac{\beta\Delta C}{Sc}\right)},$$

$$C=\frac{\bar{C}-C_L}{C_H-C_L},$$

$$Ek=\frac{v}{\Omega H^2},\quad Ro_S=\beta\Delta C,\quad Sc=\frac{v}{D},\quad Ar=\frac{H}{R},\quad Ac=\frac{R\Omega^2}{g} \tag{1}$$

The dimensionless equations in a cylindrical coordinate system rotating with angular speed Ω around its axis are as follows.

Continuity equation

$$\frac{1}{r}\frac{\partial}{\partial r}(ru)+\frac{\partial w}{\partial z}=0 \tag{2}$$

Momentum equations

$$u\frac{\partial u}{\partial r}+w\frac{\partial u}{\partial z}-\frac{v^2}{r}=2\frac{Sc}{(Sc\,Ro_S)^{1/2}}v+Sc\,rC-\frac{\partial p}{\partial r}+\frac{Sc\,Ek\,Ar^2}{(Sc\,Ro_S)^{1/2}}\nabla^2u \tag{3}$$

$$u\frac{\partial w}{\partial r}+w\frac{\partial w}{\partial z}=-\frac{Sc}{Ac}C-\frac{\partial p}{\partial z}+\frac{Sc\,Ek\,Ar^2}{(Sc\,Ro_S)^{1/2}}\nabla^2w \tag{4}$$

$$u\frac{\partial v}{\partial r}+w\frac{\partial v}{\partial z}+\frac{vu}{r}=-2\frac{Sc}{(Sc\,Ro_S)^{1/2}}u+\frac{Sc\,Ek\,Ar^2}{(Sc\,Ro_S)^{1/2}}\nabla^2v \tag{5}$$

Species equation

$$u\frac{\partial C}{\partial r}+w\frac{\partial C}{\partial z}=\frac{Ek\,Ar^2}{(Sc\,Ro_S)^{1/2}}\nabla^2C \tag{6}$$

The Coriolis force terms appear in the radial and azimuthal momentum equations (the first terms on the right sides of Eqs. (3) and (5)). The centrifugal and gravitational force terms appear in the radial (Eq. (3)) and vertical (Eq. (4)) momentum equations, respectively.

Since the coordinates are attached to the rotating cell, the wall velocities are zero everywhere. The normal velocity from the surfaces of cathode or anode due to the transfer of cupric ions has been found to be negligible. Due to the limiting current condition, the concentration is assumed to be zero at the cathode, and twice the bulk concentration at the anode [9]. The vertical cylindrical wall is insulated for mass transfer. Then, the dimensionless boundary conditions are:

$$z=0,\quad u=0,\quad w=0,\quad v=0,\quad C=1 \tag{7}$$

$$z=\frac{H}{R},\quad u=0,\quad w=0\quad v=0,\quad C=0 \tag{8}$$

$$r=1,\quad u=0,\quad w=0,\quad v=0,\quad \frac{\partial C}{\partial r}=0 \tag{9}$$

$$r=0,\quad \frac{\partial u}{\partial r}=0,\quad \frac{\partial w}{\partial r}=0,\quad \frac{\partial v}{\partial r}=0,\quad \frac{\partial C}{\partial r}=0 \tag{10}$$

The boundary conditions at $r=0$ are axisymmetry.

A control volume, finite difference method with the power law scheme is used to discretize the equations and boundary conditions. The coupled non-linear algebraic equations are solved using the SIMPLEC scheme [10]. Non-uniform grid spacing is used in both r and z-directions with the minimum grid spacing being smallest near the horizontal and vertical walls and increasing exponentially away from the walls. Since high $Sc\ Ro_S$ number and low Ek number range is studied in the present work, very thin Ekman layer and solutal boundary layer exist near the electrode walls. This situation requires sufficiently fine grids inside the boundary layers.

The iterative calculation is continued until relative convergence criteria are met for all the field variables of the problem. The relative convergence criteria are as follows:

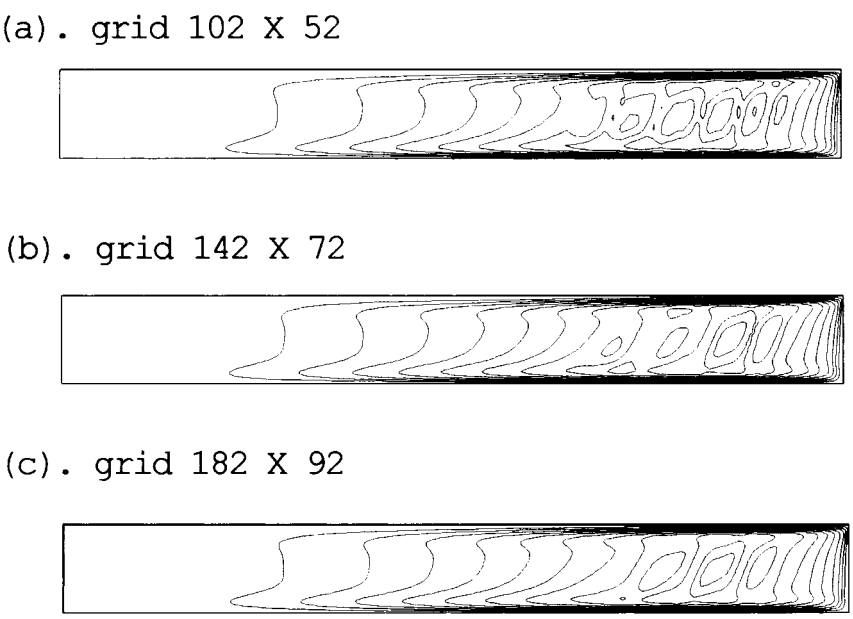

Fig. 2. Meridional streamline contours obtained with different grid systems for $Ek = 0.0057$, $Sc\ Ro_S = 10.63$, $Ar = 0.033$ (vertical scale 3×).

$$\frac{|\phi_{i,j}^{n+1} - \phi_{i,j}^{n}|_{\max}}{|\phi_{i,j}^{n}|_{\max}} < 10^{-4} \tag{11}$$

Furthermore, the steady-state solutions are checked such that the mass balance of cupric ion species between the two electrodes is within 1%. A typical number of iterations required to obtain a fully converged solution are approximately 3000 iterations for simple flows at low Ek, and more than 5000 iterations for complex flows at relatively low Ek.

The Sherwood number is calculated after the convergence is attained. The local Sherwood number at the electrode surface is defined as

$$Sh(r) = \frac{h_m(r)H}{D} = -\left.\frac{\partial C}{\partial z}\right|_{\text{wall}} \times \frac{H}{R} \tag{12}$$

The total Sherwood number is obtained by integrating the local value in the r-direction,

$$\overline{Sh} = 2\int_0^1 r\, Sh(r)\, \mathrm{d}r \tag{13}$$

Three grid systems, 102 × 52, 142 × 72, 182 × 92, are used to test their effects on the total Sherwood number and the minimum stream function. For the case of $Ek = 0.0115$ and $Sc\ Ro_S = 10.63$, the Sherwood numbers are 4.51, 4.52, 4.53, and the minimum stream functions are -3.92×10^{-4}, -3.93×10^{-4}, -3.93×10^{-4}, respectively. For the case of $Ek = 0.0057$ and $Sc\ Ro_S = 10.63$, the Sherwood numbers are 6.43, 6.46, 6.48, and the minimum stream functions are -2.91×10^{-4}, -2.93×10^{-4}, -2.94×10^{-4}, respectively. The maximum variation of Sherwood number for the different grid systems is less than 0.8%. The computed mass transfer rates are within the error of experimental data in [6], as will be shown later. Therefore, the grid system of 102 × 52 is judged to be adequate for the mass transfer rate study.

The flow pattern is also sensitive to the grid resolution. An especially complex flow appears in the core region under certain conditions. In this situation, the computational mesh must be sufficiently fine to resolve the flow feature. For the case of $Ek = 0.0115$ and $Sc\ Ro_S = 10.63$, the flow pattern is unicellular in the r-z plane and it is found that the 102 × 52-grid system provides good resolution for the flow and concentration patterns. At $Ek = 0.0057$, however, it becomes difficult to resolve the flow structure accurately because a complex flow structure appears with a series of secondary cells. In that situation, the computed streamline pattern changes with the grid system employed, as shown in Fig. 2. However, the flow structure appears to converge to the one computed by the 182 × 92-system. Although a finer grid system than the 182 × 92-system is not tested in the present study, the 182 × 92-system is judged to be adequate to reveal the details of the flow.

3. Results and discussion

The following ranges of dimensionless parameters

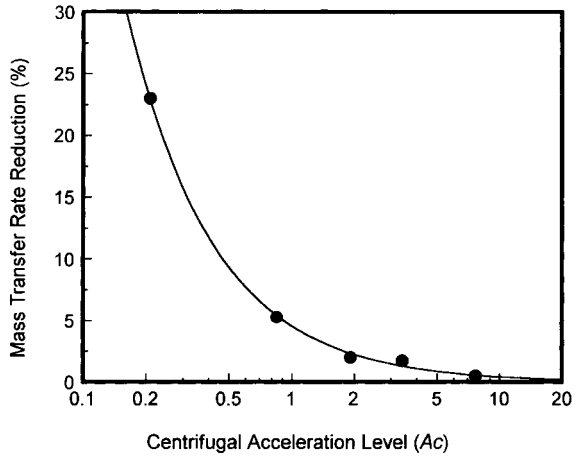

Fig. 3. Mass transfer rate percentage reduction due to gravity at different centrifugal acceleration level.

are investigated in the numerical study: $Ek = 2.8 \times 10^{-3}$ to 1.15×10^{-2}, $Sc\ Ro_S = 0.00532$ to 42.5, $Ar = 0.033$, and $Sc = 2380$. These ranges are chosen mainly to simulate the rotating nickel–zinc battery [6] but the range of $Sc\ Ro_S$ is wider than in [6] in order to study the effect of this important parameter in more general conditions.

When the electrochemical cell is operated at a high rotation speed, the buoyancy force due to gravity may be neglected. First, the present study provides a criterion for negligible gravitational buoyancy based on the relative centrifugal acceleration level (Ac). The mass transfer rates are computed under various rotation rates with and without gravity. In the present configuration, heavier fluid is near the bottom, leading to a gravitationally stable situation. Hence, gravity tends to retard the centrifugal convection and reduces the mass transfer rate. Fig. 3 presents the computed percentage reduction in mass transfer rate due to gravity as a function of Ac. The figure shows that gravity suppresses the mass transfer rate, with more reduction with decreasing Ac. At $Ac = 0.21$ gravity decreases the mass transfer rate by 23%, while at $Ac = 1.9$, the reduction is only 2%. Therefore, one can conclude that the effect of gravity on the total mass transfer rate is negligible if Ac is above about 2. In our experiment in [6], Ac ranged from 1.9 to 50.

With negligible buoyancy due to gravity the primary forces controlling the convection mechanism are the centrifugal and Coriolis forces. Then, according to our earlier scaling analysis [6], the Ek and $Sc\ Ro_S$ numbers are the primary dimensionless parameters to determine the mass transfer process. In the following, detailed flow and solutal fields are discussed for various values of Ek and $Sc\ Ro_S$.

3.1. Effect of Ek

In the present work, the overall flow and solutal fields are described by the streamlines, contours of constant azimuthal velocity, and iso-solutal lines in a r–z plane. The results obtained for two different values of Ek for a fixed $Sc\ Ro_S$ are presented in Fig. 4. In both cases Ek is less than unity so that thin viscous boundary layers, called the Ekman layers, exist along the top and bottom walls. The region sandwiched between these boundary layers is called (inviscid) the core region herein. According to our scaling analysis [6]; (i) the boundary layer becomes thinner as Ek becomes smaller, (ii) the centrifugal buoyancy and viscous forces are balanced in the boundary layer, and (iii) the Coriolis force dominates in the core region.

Fig. 4a shows the flow and concentration fields for relatively large Ek ($= 0.0115$). The core flow in a radial cross-section is mainly unicellular with counterclockwise circulation. The cell center is located near the outer edge. The relatively heavy fluid near the bottom electrode flows radially outward with its velocity increasing with radius due to increasing centrifugal force. Consequently, the bottom boundary layer entrains fluid from the core region as it moves radially outward. The opposite happens for the boundary layer along the top electrode, detraining fluid from there to the core region. As a result, there is a net axial flow from the top to the bottom boundary layer, called the Ekman suction, except near the outer edge where the flow must turn upward. That results in counterclockwise circulation in a fixed radial plane.

The iso-solutal lines in Fig. 4a show that solutal boundary layers exist on the top and bottom electrodes. Centrifugal buoyancy exists mainly in these layers. The solutal boundary layer on the top electrode starts from the outer edge and increases its thickness rapidly, because the flow is decelerating as it moves inward (or because the Ekman suction flow convects concentration from the top to the bottom electrodes). Consequently, the mass transfer rate at the top electrode is very high near the outer edge. The top boundary layer becomes very thick inside the half-radius position. Therefore, there is a region of low cupric ion concentration near the center of cylinder cell. On the other hand, the solutal layer thickness along the bottom electrode is nearly constant over the surface. The iso-solutal lines in the core region show that the solution there is nearly stratified in the radial direction.

Fig. 4a also shows the azimuthal velocity distribution. The azimuthal velocity is induced by the azimuthal component of the Coriolis force, which is proportional to $-u$ (see Eq. (5)). Consequently, the azimuthal velocity is positive (negative) in the region where the radial velocity is negative (positive). The azimuthal velocity is positive over the top electrode,

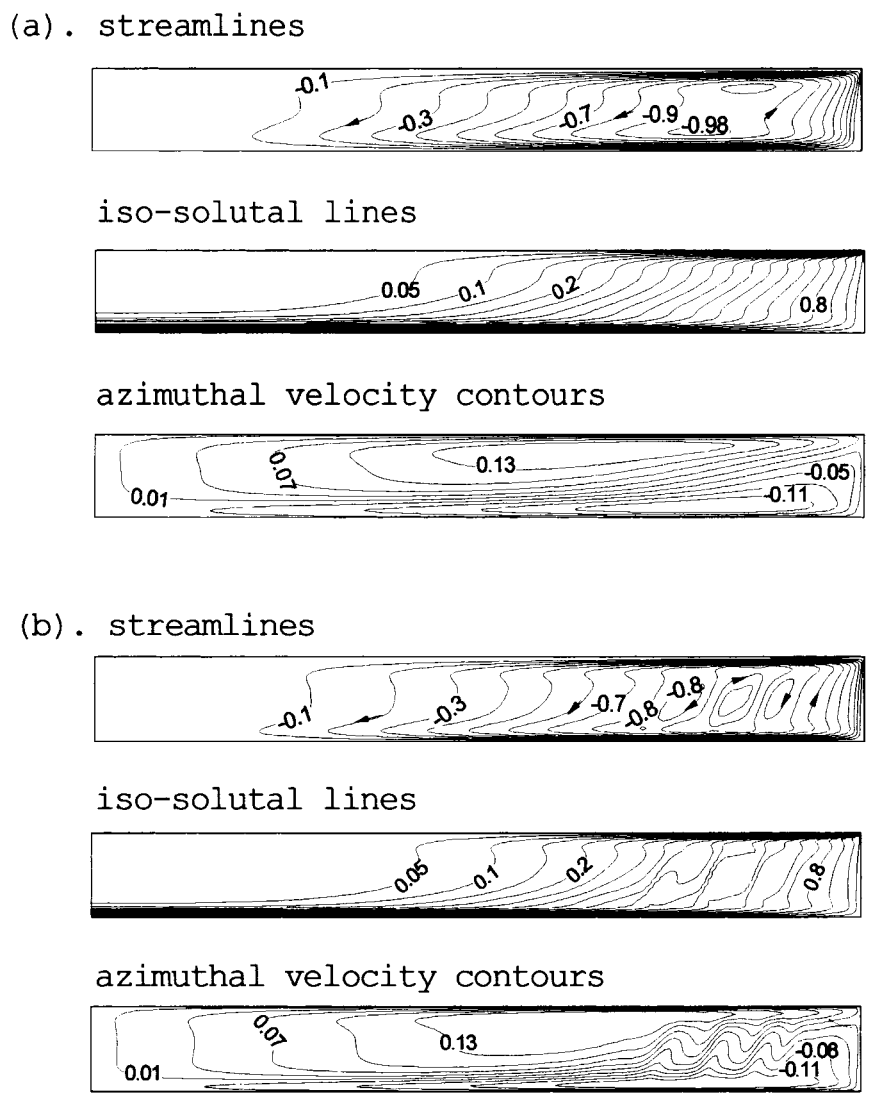

Fig. 4. Contour plots of meridional streamlines, iso-solutal lines and azimuthal velocities for (a) $Ek = 0.0115$, (b) $Ek = 0.0057$, and for $Sc\ Ro_S = 10.63$, $Ar = 0.033$ (vertical scale 3×).

meaning that the fluid there rotates faster than the cell. The fluid over the bottom electrode rotates slower. Since the Coriolis force dominates in the core, the azimuthal velocity is large in the core. The radial component of the Coriolis force is proportional to the azimuthal velocity (Eq. (3)). With the above azimuthal velocity distribution, the radial Coriolis force opposes the centrifugal buoyancy in the solutal boundary layers, namely the Coriolis force generates clockwise circulation, which results in reduced convection in a radial cross-section.

When Ek is reduced to 0.0057 (Fig. 4b), a series of reverse cells with clockwise circulation appear and they interact with the primary flow in the Ekman layers. As Ek decreases, the boundary layers become thinner and the core region expands. Consequently, the Coriolis force, which dominates in the core, becomes increasingly important relative to the centrifugal buoyancy. As mentioned above, the radial Coriolis force opposes centrifugal buoyancy, so when Ek becomes small enough, the flow direction is reversed in some part of the core region.

Fig. 5 shows the Ekman number effect on the local boundary layer characteristics. The radial velocity (u) distributions are shown in Fig. 5a. The Ekman layer thickness is nearly uniform over both the top and the bottom electrodes and the average thickness is about 20% of the cell height. The thickness decreases as the

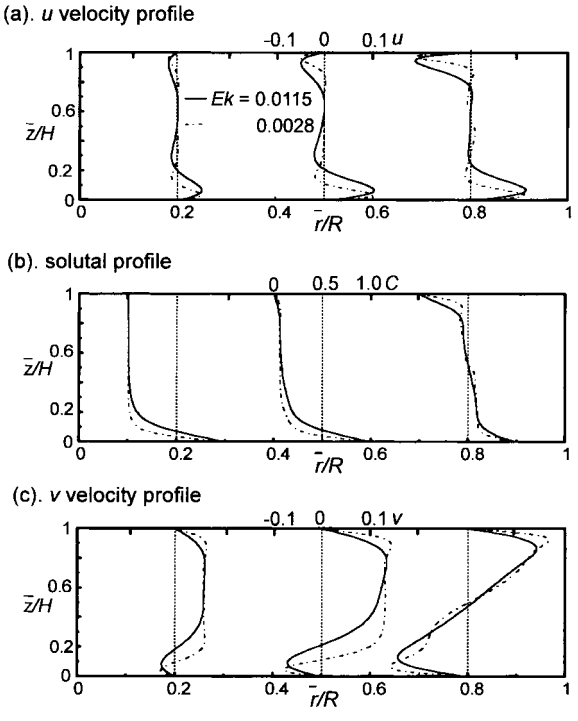

Fig. 5. Velocity and solutal profiles at $r/R = 0.2$, 0.5, 0.8 for different Ekman numbers, and for $Sc\ Ro_S = 10.63$, $Ar = 0.03$.

Ekman number decreases. The radial velocity increases with the radial distance along the bottom electrode because the centrifugal buoyancy increases in that direction. The opposite happens along the top plate. The (dimensionless) maximum velocity at a fixed radial location is not a strong function of Ek. The negative velocity outside the bottom Ekman layer is caused by the Coriolis force as it opposes the main boundary-layer flow. Fig. 5b shows that thin solutal layers exist only near the outer edge on the top electrode but almost uniformly on the bottom of the cell. In the parametric range of the present work, the solutal boundary layers are thinner than the velocity boundary layers [6]. The solutal layer thickness decreases as Ekman number decreases.

Fig. 5c shows that the azimuthal velocity is larger than the radial velocity on the average. Especially, the azimuthal velocity dominates in the core region. The reason for the difference in the velocity magnitude is that the radial velocity is reduced by the Coriolis force. In order to see the effect of the Coriolis force on the flow field, the Coriolis terms in Eqs. (3) and (5) are artificially neglected in some computations. The computed u-velocity and solute distributions with and without the Coriolis terms are compared in Fig. 6. As the figure shows, the radial velocity becomes larger

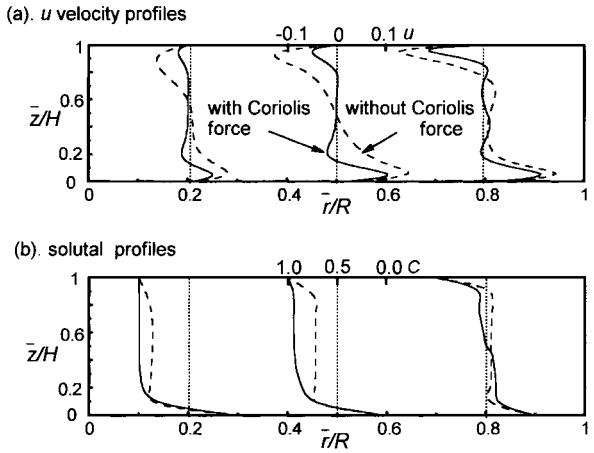

Fig. 6. Velocity and solutal profiles for $Ek = 0.0057$, $Sc\ Ro_S = 10.63$, $Ar = 0.033$, comparing between Coriolis force and zero Coriolis force.

without the Coriolis force, especially in the core region. Since the u-velocity distribution is no longer concentrated near the walls without the Coriolis force, the solutal boundary layer is less affected by the Ekman suction flow so that the solutal boundary layer along the top electrode remains over a larger area, as seen in Fig. 6.

3.2. Effect of $Sc\ Ro_S$

According to our earlier scaling analysis, the parameter $Sc\ Ro_S$ characterizes the ratio of Ekman to solutal boundary layer thickness, the ratio being given as $(Sc\ Ro_S)^{1/4}$ [6]. Since the basic velocity and solutal boundary layer characteristics have been discussed in the previous section, the focus here is on the $Sc\ Ro_S$ effects on the flow and solutal fields.

Fig. 7 shows the effect of increasing $Sc\ Ro_S$ for a fixed Ek (= 0.0115) on the overall flow and solutal fields. The most noticeable effect of the $Sc\ Ro_S$ is on the solutal field. The solutal boundary layer thickness decreases with increasing $Sc\ Ro_S$ but the velocity boundary layer thickness does not change in Fig. 7 because Ek is fixed. As the solutal boundary becomes thinner relative to the viscous boundary layer with increasing $Sc\ Ro_S$, the former becomes less influenced by the Ekman suction associated with the latter. Consequently, the solutal boundary layer on the top electrode remains over a larger area and the concentration distribution in the core spreads more into the central region at large $Sc\ Ro_S$. In other words, the core is less stratified. Fig. 7a suggests that the mass transfer at the top electrode is concentrated in a very small area near the outer edge at $Sc\ Ro_S = 5$. In comparison, the overall flow structure (both radial and azi-

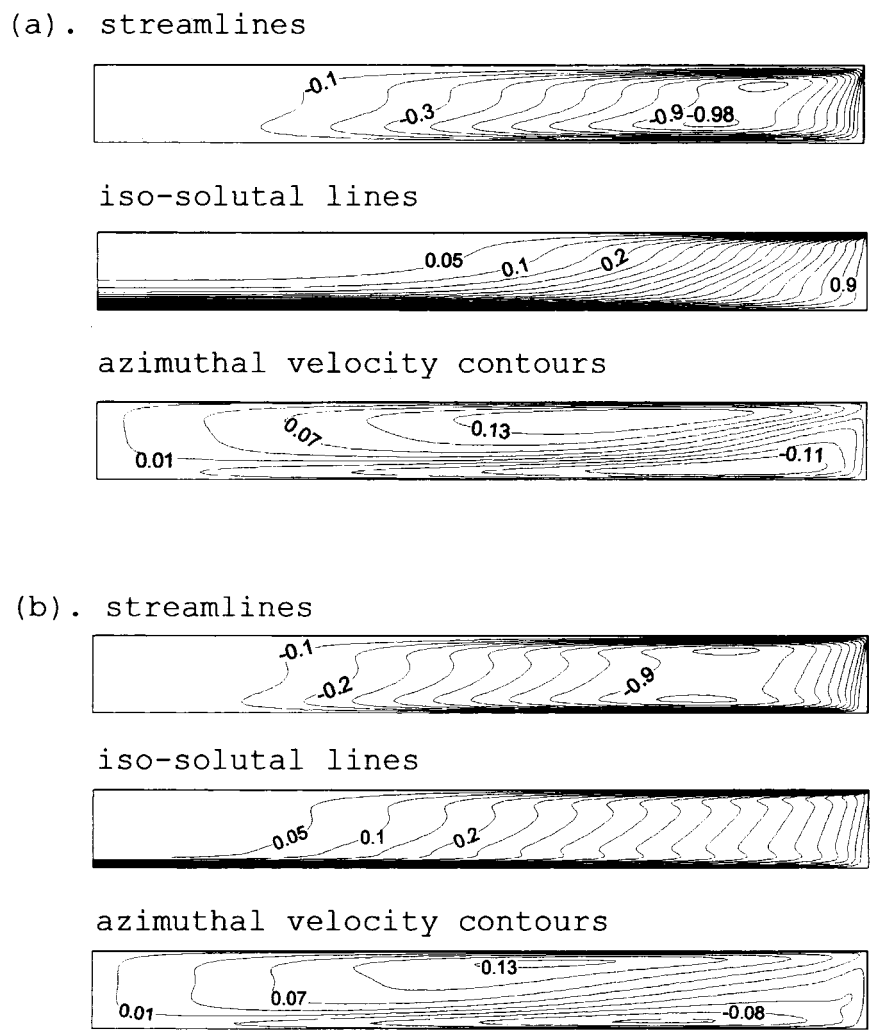

Fig. 7. Contour plots of meridional streamlines, iso-solutal lines and azimuthal velocities for (a) $Sc\ Ro_S = 5.32$, (b) $Sc\ Ro_S = 42.5$, and for $Ek = 0.0115$, $Ar = 0.033$ (vertical scale 3×).

muthal velocity fields) does not change appreciably when $Sc\ Ro_S$ is varied.

Fig. 8 presents the local velocity and solutal profiles for different $Sc\ Ro_S$ at $r/R = 0.2$, 0.5 and 0.8. The solutal boundary layer thickness decreases with increasing $Sc\ Ro_S$ (Fig. 8b) and, as a result, the location of peak radial velocity gets closer to the wall and the maximum radial velocity increases (Fig. 8a). However, the overall Ekman layer thickness (the region of positive (negative) radial velocity next to the bottom (top) electrode) is not appreciably affected by $Sc\ Ro_S$ (Fig. 8a), which is consistent with our scaling analysis [6]. As seen in Fig. 8c, the azimuthal velocity is affected by $Sc\ Ro_S$ mainly near the outer edge where it decreases with increasing $Sc\ Ro_S$. As the main driving force regions move closer to the walls with increasing $Sc\ Ro_S$, the viscous retardation effect of the walls on the azimuthal velocity increases, thus decreasing the velocity.

If Ek is reduced to 0.0057, a secondary flow will appear in the core region, as discussed earlier. It is found that if the $Sc\ Ro_S$ were increased in that situation, it would become more difficult to obtain a converged solution. Experimentally, the flow field is known to become time-dependent when $Ek = 0.0043$ and $Sc\ Ro_S = 21$ [6]. As $Sc\ Ro_S$ becomes large, the core is less (stably) stratified, as discussed above, so that if Ek is small, the opposing interaction between the Coriolis force and centrifugal buoyancy could make the flow unstable. More work is needed to understand this transition phenomenon.

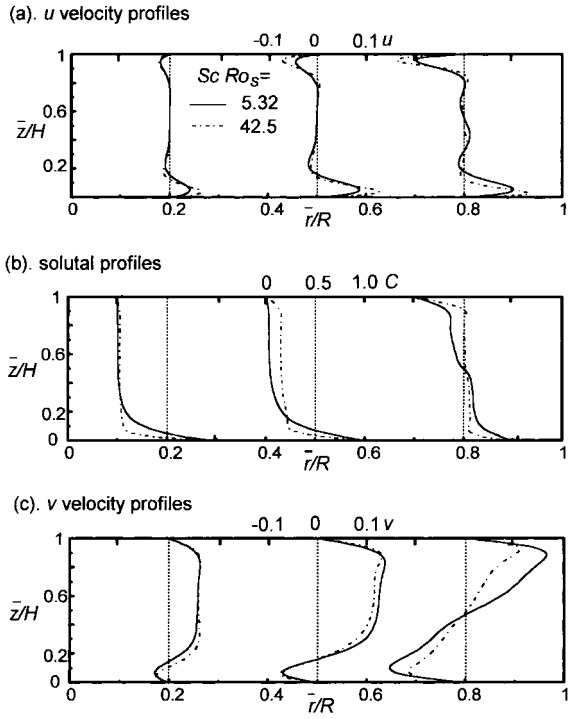

Fig. 8. Velocity and solutal profiles at $r/R = 0.2, 0.5, 0.8$ for different $Sc\ Ro_S$ and for $Ek = 0.0115$, $Ar = 0.033$.

3.3. Mass transfer rate

Finally, the effect of Ek and $Sc\ Ro_S$ on the mass transfer rate is discussed. According to our scaling analysis [6], the dimensionless mass transfer rate, the Sherwood number (Sh), scales with $Ek^{-1/2}(Sc\ Ro_S)^{1/4}$ when $Sc\ Ro_S$ is much larger than unity. For this reason, $\overline{Sh}\,Ek^{1/2}$ is plotted against $Sc\ Ro_S$ for different Ek values in Fig. 9. The experimental data from [6] are also shown in the figure for comparison. The difference between them is all within the experimental error, which is $\pm 8\%$. The figure shows that $\overline{Sh}\,Ek^{1/2}$ is closed to $(Sc\ Ro_S)^{1/4}$ beyond about $Sc\ Ro_S = 5$ and the experimental data lie in that region. The solutal boundary layers disappear when $Sc\ Ro_S$ becomes much less than unity so that Sh becomes equal to unity or $\overline{Sh}\,Ek^{1/2}$ becomes equal to $Ek^{1/2}$. The streamlines, solute and azimuthal velocity distributions for $Sc\ Ro_S = 0.53$ and $Ek = 0.0057$ are presented in Fig. 10, which shows that although the concentration variation in the axial direction is linear over most of the cell, the solute distribution is distorted near the outer edge. Since Ek is less than unity in Fig. 10, the velocity boundary layers still exist even when the mass transfer is diffusion controlled so that the flow along the bottom electrode turns upward in a relatively small region next to the outer wall. Consequently, convection by the turning flow, which is in the direction of large concentration gradients, is important in the corner and a solutal boundary layer appears in the top corner.

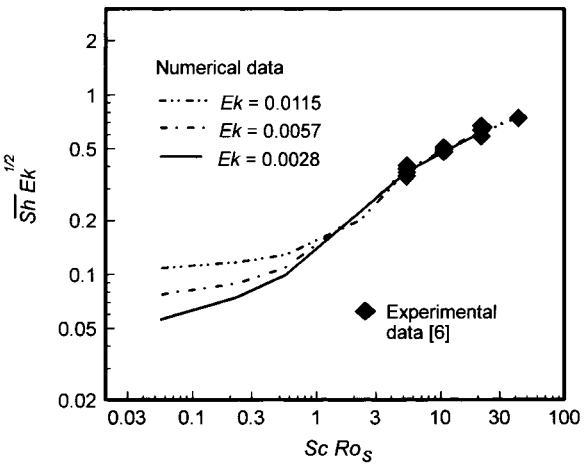

Fig. 9. $\overline{Sh}\,Ek^{1/2}$ vs. $Sc\ Ro_S$ for numerical and experimental data.

Fig. 11 shows the effect of the Coriolis force on the Sherwood number as a function of $Sc\ Ro_S$ for a fixed value of Ek. As discussed earlier, the Coriolis force reduces the radial velocity because it opposes the centrifugal buoyancy. Therefore, the mass transfer rate is also reduced by the Coriolis force in the parametric range where the Coriolis force is not negligible compared to the centrifugal buoyancy. With increasing $Sc\ Ro_S$, the solutal boundary becomes thinner relative to the Ekman layer so that the mass transfer rate is affected less by the Coriolis force. Fig. 11 suggests that the effect of Coriolis force becomes negligible just beyond the maximum value of $Sc\ Ro_S$ in the present computation. In the case of zero Coriolis force there is no azimuthal velocity, hence the flow recirculates in a fixed radial plane. Thus, the centrifugal convection in that situation is similar to buoyancy-driven convection so that Sh is proportional to the 1/4th power of $Sc\ Ro_S$ for a given Ek [6], as can be seen in Fig. 11.

On the other hand, when $Sc\ Ro_S$ is very small, the mass transfer is by diffusion so that Sh is unity with or without the Coriolis force. The maximum reduction of Sh by the Coriolis force occurs around $Sc\ Ro_S$ of unity for $Ek = 0.0057$ according to Fig. 11. The maximum reduction is about 50%. Therefore, one practical way to increase the mass transfer rate is to reduce the azimuthal flow by using, for example, partitions. This aspect is being investigated currently.

The local mass transfer rate is shown in Fig. 12. All the distributions in Fig. 12 are slightly wavy near the outer edge due to the secondary cells. The mass transfer rate is relatively uniform along the bottom electrode but very concentrated near the outer edge on the

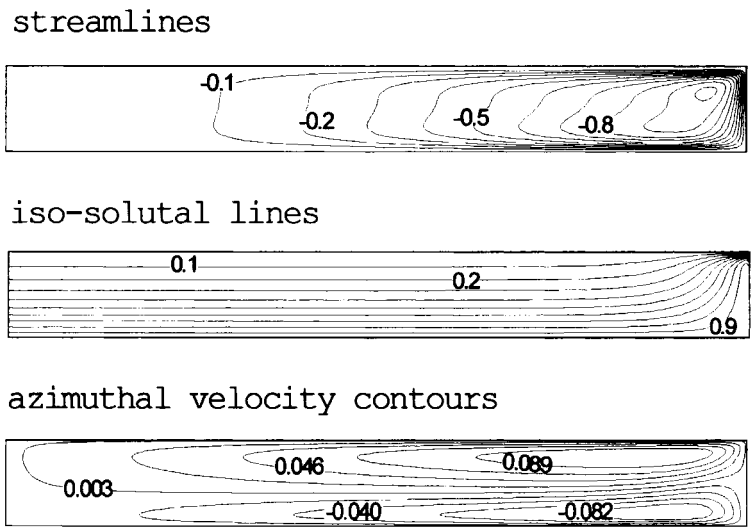

Fig. 10. Contour plots of meridional streamlines, iso-solutal lines and azimuthal velocities for $Sc\ Ro_S = 0.53$, $Ek = 0.0057$, $Ar = 0.033$ (vertical scale 3×).

top electrode. The fact that the mass transfer rate is very high near the top electrode edge is in agreement with the copper deposition pattern that observed experimentally [11]. This is not an efficient use of cathode surface because only a portion of it is utilized. One effective way to spread the mass transfer on the cathode is to reduce the azimuthal velocity, as was discussed earlier in conjunction with Fig. 6. On the other hand, the non-uniform mass transfer may be utilized to control the shape change phenomenon on the zinc electrode (cathode) of Ni/Zn battery. The zinc material is known to deplete from the edge area, thereby reducing the mass transfer there [12]. Therefore, by increasing the mass transfer in the edge area, it may be possible to minimize the shape change. More work is needed to optimize the present basic concept for efficient battery design.

4. Conclusions

Solutal convection in rotating electrochemical cells has been studied numerically. A shallow circular cell ($Ar = 0.033$) is rotated around its axis with cathode on the top. The gravitational force is negligible as the centrifugal acceleration level relative to gravity is larger than about 2. The effects of two important dimensionless parameters, Ek and $Sc\ Ro_S$, on the flow and solutal fields are investigated. The results show complex interactions between the centrifugal buoyancy and

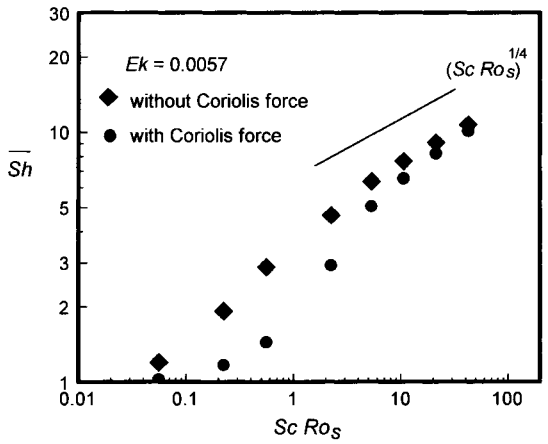

Fig. 11. Total Sherwood number vs. $Sc\ Ro_S$ for $Ek = 0.0057$ with and without Coriolis force.

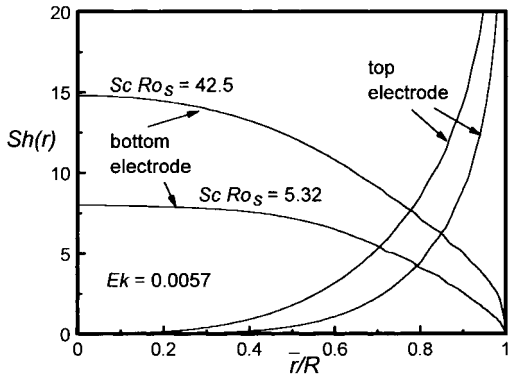

Fig. 12. Local Sherwood number distribution for different $Sc\ Ro_S$, and for $Ar = 0.033$, $Ek = 0.0057$.

Coriolis force. The Coriolis force generates relatively strong azimuthal velocity in the present parametric range and suppresses the centrifugal convection in a radial plane. When Ek is larger than about 0.01, the core flow is unicellular, sandwiched by the top and the bottom Ekman layers. When the Ek becomes less than about 0.006, a series of secondary cells appear in the core, which are induced by the Coriolis force. A solutal boundary layer exists only over a relatively small region near the outer edge on the cathode in the present parametric range so that the local mass transfer is more concentrated in that region. The result could be utilized to control the shape change of nickel–zinc battery and prolong its life-cycle. The Coriolis force reduces the mass transfer rate, especially near $Sc\ Ro_S$ of unity. The mass transfer can be increased by suppressing the azimuthal velocity, which also makes the mass transfer on the cathode more uniform.

Acknowledgements

We would like to acknowledge gratefully the financial support by NASA's Office of Life and Microgravity Science and Applications under grant NAG3-886.

References

[1] P. Tamminen, A.J. Salkind, High power density longlife bipolar nickel–zinc batteries in power source 12-proc, in: International Power Sources Conference 16, Brighton, England, 1988.

[2] A.J. Salkind, E. Kantner, C. Grun, Diffusion limitations to cycle life of nickel–zinc batteries and effects of vibration and rotation, Proceedings of Symposium on Rechargeable Zinc Batteries 95 (14) (1995) 160–181.

[3] H.P. Greenspan, The Theory of Rotating Fluids, Cambridge University Press, Cambridge, 1969.

[4] D. Dijktra, G.J.F. van Heijst, The flow between two finite rotating disks enclosed by a cylinder, Journal of Fluid Mechanics 128 (1983) 123–154.

[5] R. Hide, P.J. Mason, Sloping convection in a rotating fluid, Advances in Physics 24 (1975) 47–100.

[6] F.-B. Weng, Y. Kamotani, S. Ostrach, Mass transfer rate study in rotating shallow electrochemical cells, International Journal of Heat and Mass Transfer 41 (1998) 2725–2733.

[7] Z.Y. Guo, C.M. Zhang, Thermal drive in centrifugal fields; mixed convection in a vertical rotating cylinder, International Journal of Heat and Mass Transfer 35 (1992) 1635–1644.

[8] J. Chew, Computation of convection laminar flow in rotating cavities, Journal of Fluid Mechanics 153 (1985) 339–360.

[9] Y. Kamotani, L.W. Wang, S. Ostrach, H.D. Jiang, Experimental study of natural convection in shallow enclosures with horizontal temperature and concentration gradients, International Journal of Heat and Mass Transfer 28 (1985) 165–173.

[10] J.P. Doormael, G.D. Raithby, Enhancement of the SIMPLE method for predicting imcompressible fluid flows, Numerical Heat Transfer 7 (1984) 147–163.

[11] F.B. Weng, Mass transport process in rotating shallow electrochemical cells, Ph.D. thesis, Case Western Reserve University, Cleveland, OH, January 1997.

[12] R.E.F. Einerhand, W. Visscher, J.J.M. de Goeij, E. Barendrecht, Zinc electrode shape change II. Process and mechanism, Journal of the Electrochemical Society 138 (1) (1991) 7–17.